

Lawrence Berkeley National Laboratory

LBL Publications

Title

Roll-to-Roll Printed Large-Area All-Polymer Solar Cells with 5% Efficiency Based on a Low Crystallinity Conjugated Polymer Blend

Permalink

<https://escholarship.org/uc/item/3003q08b>

Journal

Advanced Energy Materials, 7(14)

ISSN

1614-6832

Authors

Gu, Xiaodan
Zhou, Yan
Gu, Kevin
et al.

Publication Date

2017-07-01

DOI

10.1002/aenm.201602742

Peer reviewed

Roll-to-Roll Printed Large-Area All-Polymer Solar Cells with 5% Efficiency Based on a Low Crystallinity Conjugated Polymer Blend

Xiaodan Gu, Yan Zhou, Kevin Gu, Tadanori Kurosawa, Yikun Guo, Yunke Li, Haoran Lin, Bob C. Schroeder, Hongping Yan, Francisco Molina-Lopez, Christopher J. Tassone, Cheng Wang, Stefan C. B. Mannsfeld, He Yan, Dahui Zhao, Michael F. Toney,* and Zhenan Bao*

The challenge of continuous printing in high-efficiency large-area organic solar cells is a key limiting factor for their widespread adoption. A materials design concept for achieving large-area, solution-coated all-polymer bulk heterojunction solar cells with stable phase separation morphology between the donor and acceptor is presented. The key concept lies in inhibiting strong crystallization of donor and acceptor polymers, thus forming intermixed, low crystallinity, and mostly amorphous blends. Based on experiments using donors and acceptors with different degree of crystallinity, the results show that microphase separated donor and acceptor domain sizes are inversely proportional to the crystallinity of the conjugated polymers. This methodology of using low crystallinity donors and acceptors has the added benefit of forming a consistent and robust morphology that is insensitive to different processing conditions, allowing one to easily scale up the printing process from a small-scale solution shearing coater to a large-scale continuous roll-to-roll (R2R) printer. Large-area all-polymer solar cells are continuously roll-to-roll slot die printed with power conversion efficiencies of 5%, with combined cell area up to 10 cm². This is among the highest efficiencies realized with R2R-coated active layer organic materials on flexible substrate.

1. Introduction

Solar cells hold great promise as a dominant renewable energy source for human society.^[1,2] Organic solar cells are intended for high throughput, low-cost manufacturing on flexible substrates.^[3] Their capital and energy payback time is estimated to be much shorter compared to silicon solar cells.^[4] The low cost combined with flexible cells may find applications as building integrated or wearable photovoltaics. While there are several challenges to make organic solar cells a viable technology, impressive improvements to the efficiencies of organic solar cells have been made through optimizing active layer absorption, energy level matching, and morphology control.^[1,5–7] A major challenge remains in the lack of consistent control of the solar cell morphology during the solution printing process, since the bulk heterojunction (BHJ) active layer

Dr. X. Gu,^[†] Dr. Y. Zhou, K. Gu, Dr. T. Kurosawa,
Dr. B. C. Schroeder,^[††] Dr. F. Molina-Lopez, Prof. Z. Bao
Department of Chemical Engineering
Stanford University
Stanford, CA 94305, USA
E-mail: zbao@stanford.edu

Dr. X. Gu, Dr. H. Yan, Dr. C. J. Tassone, Dr. M. F. Toney
Stanford Synchrotron Radiation Lightsource
SLAC National Accelerator Laboratory
Menlo Park, CA 94025, USA
E-mail: mftoney@slac.stanford.edu

Y. Guo, Prof. D. Zhao
College of Chemistry
Peking University
Beijing 100871, China

Y. Li, H. Lin, Prof. H. Yan
Department of Chemistry and
Hong Kong Branch of Chinese National Engineering Research Center
for Tissue Restoration & Reconstruction
Hong Kong University of Science and Technology
Clear Water Bay, Kowloon, Hong Kong

Dr. C. Wang
Advanced Light Source
Lawrence Berkeley National Laboratory
Menlo Park, CA 94025, USA
Prof. S. C. B. Mannsfeld
Center for Advancing Electronics Dresden
Dresden University of Technology
Dresden 01062, Germany



^[†]Present address: School of Polymers and High Performance Materials,
University of Southern Mississippi, Hattiesburg, MS 39406, USA

^[††]Present address: Materials Research Institute and School of Biological
and Chemical Sciences, Queen Mary University of London, Mile End
Road, London E1 4NS, UK

DOI: 10.1002/aenm.201602742

morphology is highly sensitive to different processing conditions.^[3,8,9] In a BHJ structure, donor and acceptor polymers are mixed together to form a bicontinuous interpenetrating network with large interfacial areas for efficient exciton dissociation. The BHJ active layer morphology is critical for organic solar cell device performance, since an exciton has a limited diffusion length (≈ 20 nm).^[10]

For organic BHJ solar cells, previous studies have shown that the domain size of the phase-separated donor and acceptor blends, the degree of intermixing, degree of crystallinity, and the interfacial molecular orientation all collectively affect exciton generation, transport, and dissociation, as well as charge transport, recombination, collection, and ultimately power conversion efficiency (PCE).^[11–15] To date, high-performance organic solar cells are largely fabricated by spin-coating on rigid glass substrates through labor-intensive testing of wide processing parameters. Unfortunately, the performance of solar cells based on heavily optimized spin-coating fabrication process typically deteriorates drastically when scaled up to using an industrially relevant roll-to-roll (R2R) fabrication processes.^[16]

All-polymer solar cells have been under rapid development recently as an alternative to polymer:fullerene cells. The performance of those cells has been reported to be higher than 7%.^[17–21] They are desirable in terms of versatility in molecular design to tune the absorption range and the enhanced chemical and mechanical stabilities.^[22–24] However, large phase separation between donor and acceptor polymer represents a major factor limiting the attainable device efficiencies, especially the large domain sizes observed in recent reports.^[25–27] By using a set of in situ and ex situ soft and hard X-ray scattering techniques, we found that crystallization of the donor and acceptor polymers is responsible for the large-scale phase separation in all-polymer BHJs.^[28] The large domain size, if much larger than the typical exciton diffusion length of 10–20 nm, is undesirable due to this resulting in inefficient exciton splitting.^[29] On the other hand, higher crystallinity could improve the charge carrier mobility, and thereby facilitate charge collection and enhance the fill factor.^[5] However, the enhanced charge carrier mobility is usually accompanied by the loss of exciton harvesting due to large phase separation between donors and acceptors.^[26]

It is relatively easy to enhance the polymer blend phase segregation and crystallinity by postdeposition thermal or solvent vapor annealing,^[30,31] addition of nucleation agents, and the employment of high-boiling-point (B.P.) solvent additives.^[32,33] These methods are effective for improving PCEs for some polymer solar cells systems, such as poly(3-hexylthiophene) (P3HT):phenyl-C61-butyric-acid-methyl-ester (PCBM) system, where the degree of crystallinity and phase separation upon solution processing are low (e.g., <10 nm). However, these are less effective for all-polymer solar cells, since the polymers have a tendency to form large phase separated domains after deposition (e.g., >100 nm). Additional annealing further increases domain sizes. Thus for all-polymer solar cells, there is a more pressing need to control the phase separation to improve exciton splitting into free charge carriers. This can be achieved through reducing the tendency of polymer to crystallize. For example, quenching the polymer from its melt state to inhibit its crystallization, or using low boiling point solvents to allow fast solvent evaporation are among some strategies reported.^[34]

Increasing molecular weight of conjugated polymer could also decrease its crystallinity. However, the polymers may be difficult to process due to decreased solubility.^[35]

In this work, we use in situ grazing incidence X-ray diffraction (GIXD) to characterize the domain formation during film casting process and together with resonant soft X-ray scattering (RSoXs) to determine the corresponding domain size. We found that reducing the crystallinity of conjugated polymers is an effective way to control their phase separation in the BHJ. We chose four pairs of donors and acceptors with different degrees of crystallinity. Reduced polymer crystallinity was found to help suppress the driving force for phase separation. This understanding allowed us to select donor and acceptor polymer pairs that can be coated reliably and uniformly by R2R coating with efficiency up to 5% with module size up to 10 cm². This work represents one of the highest reported PCEs for R2R-coated all-polymer solar cells.^[1,16,36–43]

2. Results

2.1. Controlling Phase Separation Size Scale by Tuning Polymer Crystallinity

Polymer crystallization is commonly observed for traditional commodity polymers, such as polyethylene and nylons.^[34] The mechanical and optical properties of a polymer are highly linked to its degree of crystallinity.^[44] Thus tuning and controlling the crystallinity of polymers has been an important topic in polymer physics for the past few decades. Similarly, this concept is important for conjugated polymer as they typically adopt semicrystalline morphology when processed from solvents, and the crystalline structure of conjugated polymer has been closely linked to their device performance.^[45–47] The crystalline domains are also important for organic solar cells since polymer crystallization is believed to be the driving force for phase separation between donor and acceptor polymer in all-polymer solar cells.^[28] Previously, we reported fluid-enhanced crystal engineering (FLUENCE) control of nucleation density to reduce domain size in all-polymer solar cells.^[23]

In this work, we first investigated the crystallization behavior of four combinations of donor and acceptor with different crystallinity by in situ GIXD. An irregular bulky polymer side chain is used to disrupt the packing of polymer chains to inhibit crystallization and form amorphous polymer blends (**Figure 1a**). We then used this amorphous polymer blend in R2R printing of all-polymer solar cells by a custom-built mini R2R coater (**Figure 1b**). The use of an irregular bulky polymer side chain is a fundamentally different way to control the phase separation from previous methods, which rely on use of kinetic trapping the polymer in a nonequilibrium state through fast solvent drying or cooling. To form crystallites, the polymer chains must pack regularly in a defined fashion in a lattice.^[44] Many factors could affect the crystallization process. For example, regioregularity has been known to strongly affect polymer packing.^[48,49] Regiorandomness prevents a polymer from forming well-ordered crystalline domains. Regiorandom P3HT showed reduced mobility in field effect transistors due to its low crystallinity.^[50] By introducing a polymer side chain regiorandomly

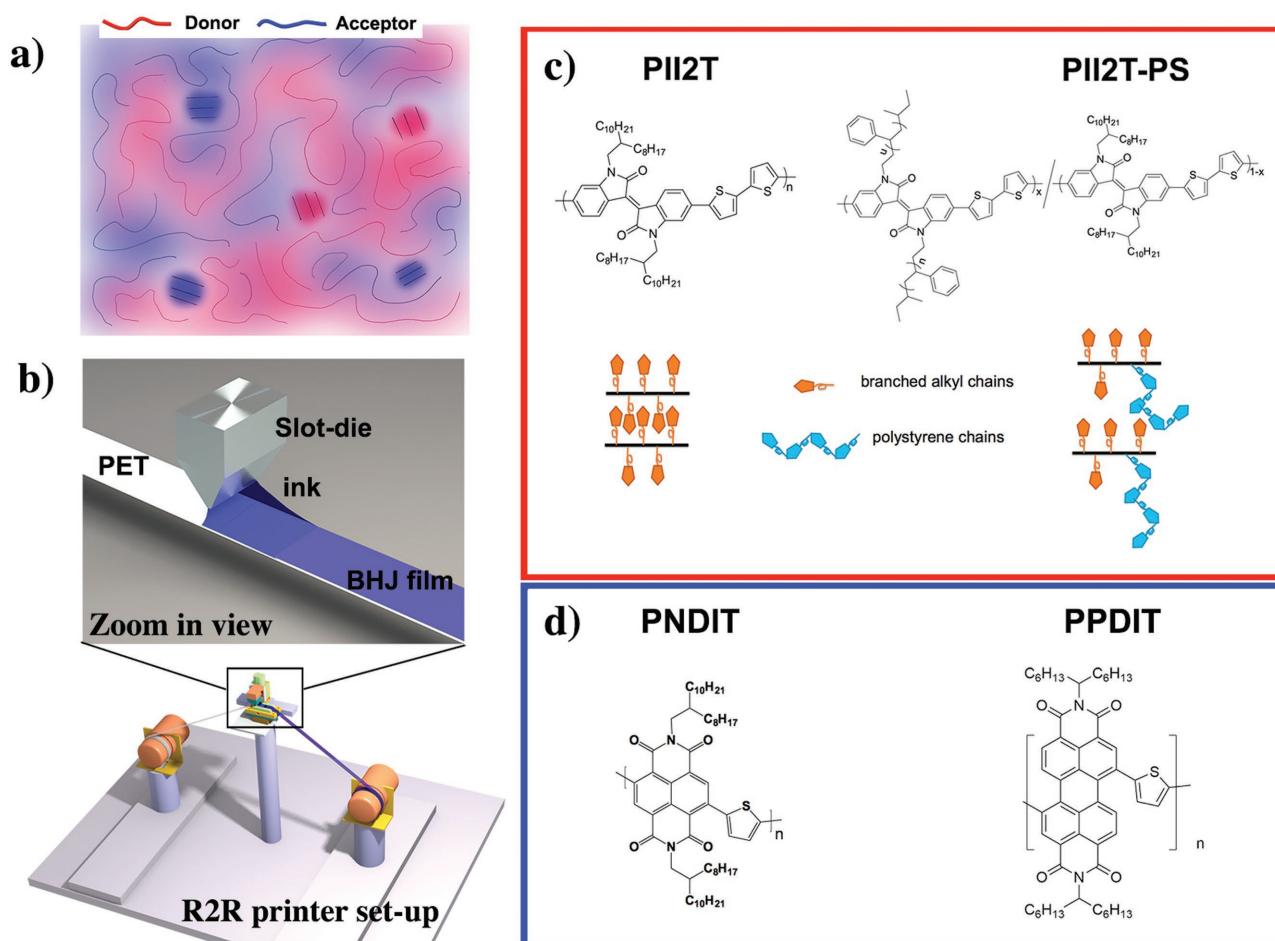


Figure 1. R2R printing of all-polymer solar cells. a) Illustration of BHJ morphology for intermixed donor and polymer chains. Red lines represent the donor chain and blue lines represent the acceptor chain. b) R2R printing using a slot die coater setup. Top figure shows the zoom-in view of the slot die coating process. c) Chemical structure of two isoindigo-based donor polymers used in this work. In the right plot, the degree of polymerization ratio between $X = 10$ determines the percentage of polystyrene (PS) side chain. Schematic of packing structure with regular branched alkyl side chains, which can form ordered crystalline domains and irregular bulky PS side chains were shown next to it, which inhibit the formation of ordered crystalline domain. d) Chemical structure of the acceptor polymers PNDIT and PPDIT.

into the backbone, the conjugated polymer is inhibited from crystallizing even when it is given sufficient time using a high boiling point solvent. The same phenomenon was reported for polyethylene polymers by using an irregular side chain.^[51]

Two isoindigo-based conjugated polymers (PII2T), one with branched alkyl side chains and the other with 90% branched alkyl side chains and 10% polystyrene (PS) randomly copolymerized (PII2T-PS) are shown in Figure 1c. In this study, the oligomeric PS side chain has a molecular weight of 1.6 kDa and polydispersity of 1.08. It has a much higher M_w than the eight and ten carbons branched alkyl side chain, which has a total molecular weight of ≈ 0.3 kDa. Such long and randomly placed PS chains (shown as cyan color) create a bulky side chain effect that we hope disturbs the regular chain packing, as shown in cartoon illustration of Figure 1c bottom. To test if PS side chains have an effect on the polymer crystalline structure, both polymers were first spin-coated on silicon substrates from chlorobenzene solutions, and characterized by GIXD, shown in Figure 2a,b. The two polymers showed remarkable differences in the diffraction patterns. PII2T with highly regular

branched alkyl side chains showed a higher degree of ordering as evidenced by the sharp and numerous lamella diffraction peaks. Up to fourth order lamella diffraction (or (h00)) peaks were clearly observed near the meridian (Q_{xy} near 0). With the bulky PS side chains, the ordering of PII2T-PS was severely disrupted and thus showed only weak and broad diffraction peaks in the lamellae (100) packing direction. Due to this bulky side chain effect, the lamella peak position was increased from 0.251 \AA^{-1} (2.65 nm) for PII2T to 0.213 \AA^{-1} (2.95 nm) for PII2T-PS. Meanwhile, the full width at half maximum (FWHM) increased from 0.025 to 0.071 \AA^{-1} , indicating that the coherence length dropped by a factor of 3. We note that quantitative comparison of relative degree of crystallinity (RDoC) between different polymer crystalline structures is difficult due to different molecular packing.^[52] Thus here we only qualitatively compare the difference between the two polymers. PII2T-PS showed 70% lower integrated peak intensity after geometry correction, compared to PII2T, suggesting a significantly lower degree of crystallinity. To further confirm that the reduced integrated peak intensity for PII2T-PS is not due to a kinetically

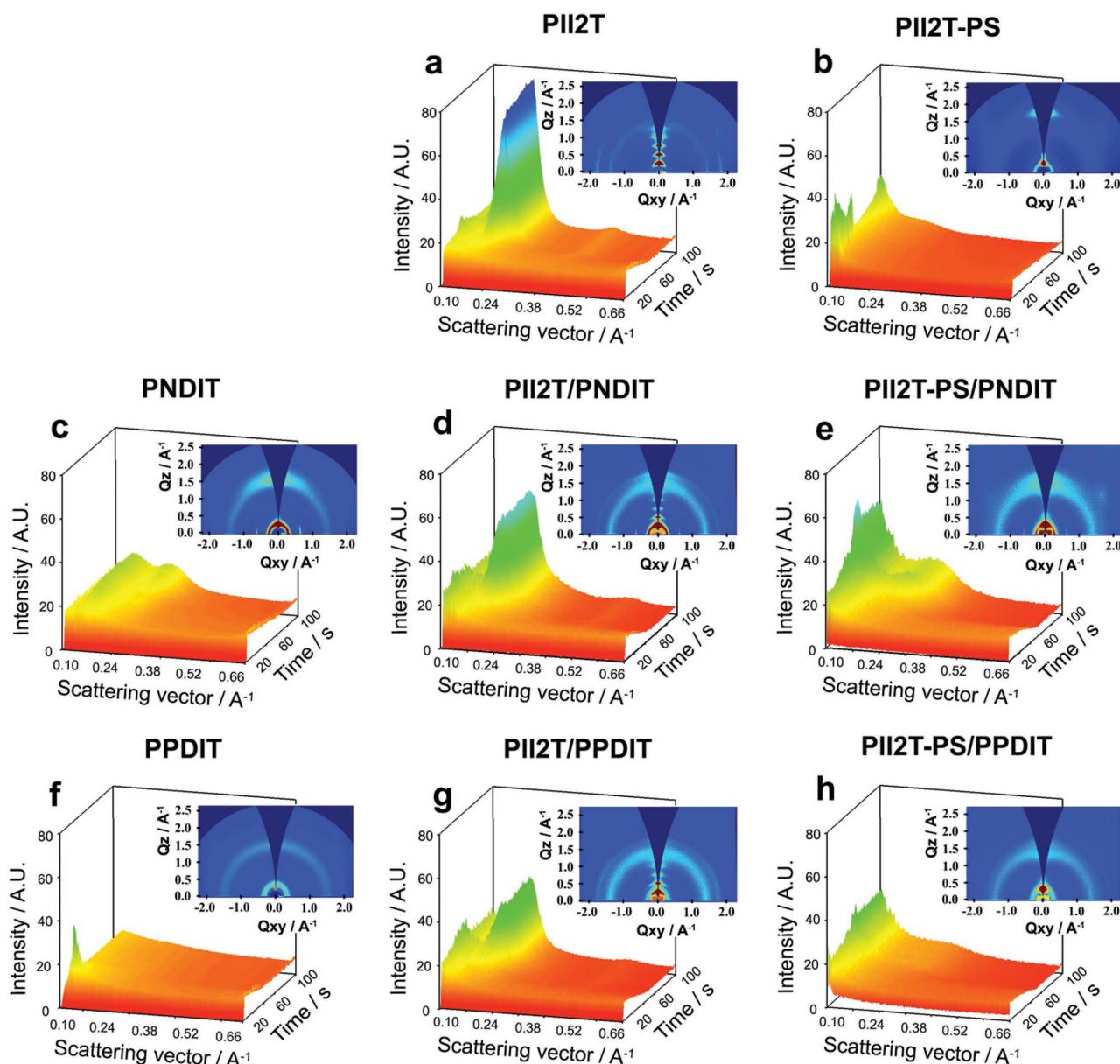


Figure 2. In situ and ex situ GIXD study of all-polymer solar cells. a,b) Two donor polymers and c,f) two acceptor polymers and their respective all-polymer solar cell blends: d) PII2T/PNDIT, e) PII2T-PS/PNDIT, g) PII2T/PPDIT, and h) PII2T-PS/PPDIT. All the in situ GIXD figures are plots of the scattering intensity with respect to scattering vectors with different drying time. The insets in the upper-right corner of each figure are the ex situ GIXD. The high crystallinity PII2T showed an intense peak (100) as well as a weak (200) in situ GIXD data, while the low crystallinity PII2T-PS showed no peaks. All the data have been normalized to the scattering volume and exposure time. Note that the intensity signal near $q = 0.1 \text{ \AA}^{-1}$ comes from specular beam and is not (100) in (h).

trapped nonequilibrium state, we measured GIXD of PII2T-PS spin-coated from a high B.P. solvent, 1,2-dichlorobenzene (ODCB) (B.P. of $180 \text{ }^\circ\text{C}$), with or without subsequent thermal annealing at $200 \text{ }^\circ\text{C}$ (see Figure S1, Supporting Information). Both samples showed similar peak positions and low extent of crystalline ordering, despite that the molecular orientation changed from face-on to edge-on when processed from ODCB with and without subsequent thermal annealing. Thus, we conclude that the PII2T-PS polymer adopts less crystalline domains (more amorphous domains) regardless of different

processing conditions, and more importantly that such a low crystallinity state is not trapped in a nonequilibrium state. This is in contrast to some other conjugated polymers. For example, when P3HT polymers are processed from a low boiling point solvent (e.g., chloroform), they are kinetically trapped into low crystallinity state.^[14,53] Upon thermal annealing or processing from a high boiling point solvent, the crystallinity of the P3HT polymer improves.

We further investigated the crystallization process of PII2T and PII2T-PS in CB using real-time X-ray diffraction during

solution shearing printing to understand the crystallization of the donor polymers during solution processing. The detailed experimental setup was reported previously.^[28] The real-time experiments were measured at 500 ms per frame continuously after the solution was sheared onto a silicon substrate. The 2D GIXD images were reduced into 1D scattering intensity versus scattering vector by using a slice cut in the out-of-plane (Q_z) direction (lamellae chain packing direction), and 3D surface plots of scattering intensity as a function of scattering vector and drying time are shown Figure 2a,b. The peak fitting and analysis were performed as previously reported.^[28] The peak position, FWHM, peak intensity, and film thickness plots are provided in Figure S2 (Supporting Information). PII2T was initially fully dissolved in the wet film (15 mg mL⁻¹). As the drying process proceeded, the polymer crystallized as indicated by the increase in the (100) diffraction intensity at a critical concentration of 30 mg mL⁻¹. The intensity steadily increased with drying time until the film was fully dried. The process is very similar to the drying process of neat P3HT as previously reported.^[28] The (200) lamella diffraction peaks were also present in the scattering profile, even at a short 500 ms exposure time. In contrast, PII2T-PS showed a much lower scattering intensity which did not show substantial increase with increased drying time (Figure 2b). Only a very weak and broad peak was observed. Data analysis based on those weak diffraction peaks was not performed due to large uncertainty in peak fitting. These in situ results combined with ex situ X-ray scattering indicate that with bulky irregular PS side chain added, the conjugated polymer showed inhibited crystallization during solution casting.

Next we investigated the crystallization behavior of the two acceptor polymers. The chemical structures of naphthalene diimide (PNDIT) and perylene diimide (PPDIT) based acceptors are shown in Figure 1d. These two polymers are chosen as they are widely used acceptor polymers in all-polymer solar cells. Two acceptors were spin-coated on silicon substrates and characterized by GIXD (Figure 2c,f inset). PNDIT shows both a smaller FWHM and higher total integrated peak intensity than PPDIT acceptors based on their alkyl (100) diffraction peak area (see Table S1, Supporting Information). Therefore, it is categorized as crystalline while PPDIT is categorized as low crystalline.

Four donor/acceptor blends were processed into BHJs to study the relationship between the phase separation size scale and their crystallinities: PII2T (crystalline)/PNDIT (crystalline), PII2T (crystalline)/PPDIT (low crystalline), PII2T-PS (low crystalline)/PNDIT (crystalline), and PII2T-PS (low crystalline)/PPDIT (low crystalline) (Figure 2d,e,g,h). The polymer solar cells were processed from 1:1 blend donor/acceptor ink in chlorobenzene at 35 °C. The (100) diffraction peak from PII2T dominated the GIXD patterns for PII2T/PNDIT (Figure 2d) and PII2T/PPDIT (Figure 2g) blends. During the drying process, the PII2T(100) lamella peak intensity increased until the film fully dried. On the other hand, no donor polymer diffraction peak was observed by in situ GIXD for PII2T-PS polymer. Only diffraction peaks from PNDIT were observed for PII2T-PS/PNDIT (Figure 2e), and no diffraction peaks were observed for PII2T-PS/PPDIT (Figure 2h). Ex situ GIXD images (Figure 2d,e,g,h insets) offer a closer look at the crystallinity for the all-polymer solar cells. A longer exposure time (180 s) improves signal-to-noise ratio. The diffraction peaks were fitted

and the results are shown in Table S1 (Supporting Information). Additionally, the crystallization of every polymer in the blend was determined to be independent for the four donor acceptor pairs (or no cocrystallite was formed) (Figure 2d,e,g,h). Line cut of the GIXD pattern in lamella packing direction at $Q_{xy} = 0$ is shown in Figure S3 (Supporting Information). The crystalline donor and acceptor polymer blends (e.g., PII2T/PNDIT) showed similar FWHM as the neat polymer scattering peaks, indicating the donor polymer maintained its crystalline state in the blend film. While in the low crystalline PII2T-PS and PPDIT blend, the FWHMs for both donor and acceptor are higher than their crystalline analogs, indicating less ordered crystalline domains.

2.2. Domain Size Characterization

The phase separation size scale in our donor and acceptor polymer blends was obtained from RSoXS (Figure 3a,c). The strongly anisotropic scattering profile is due to several reasons. First, the directional drying of polymer solution by solution shearing creates chain alignment, which was discussed in detail in our previous publication.^[54] Only the polymer chains aligned along the shearing direction could interact with the electromagnetic field.^[55] The scattering images were collected at the highest contrast between the two blended materials, which were calculated from the near-edge X-ray absorption fine structures (NEXAFS) (see Figure S4, Supporting Information). The 1D RSoXS patterns were reduced from 2D scattering profile through a cake slice in the horizontal direction (shown in Figure 3c). Additionally, a vertical cake slice and a circular average 1D diffraction profile are provided in Figure S4 (Supporting Information). The scattering in horizontal and vertical direction is slightly different, but a general trend for phase separation size scale is observed for all four polymers: that is a large phase separation size scale was found to be always associated with a high relative degree of crystallinity of at least one of the polymers in the blends. The PII2T(crystalline)/PNDIT(crystalline) showed the largest phase separation size, as evidenced by the intensity from RSoXS concentrated in the low q region (Figure 3c). When the donor in the active layer was replaced by a low crystalline polymer, PII2T-PS/PNDIT, the phase separation size scale decreased compared to both systems in which both donor and acceptors are highly crystalline. The phase separation size of all-polymer solar cells was obtained by finding the structure factor between two domains (peak in the scattering for RSoXS where a peak is observed). The peak of the scattering invariant (intensity multiply by scattering vector square $I \times q \times q$) versus scattering vector q plot were fitted to find scattering profile peak. This peak is related to the average phase separation spacing between donor and acceptor polymers. The value of phase separation size scale is shown in Table 1. Similar results were observed previously.^[23] The smallest phase separation size scale of ≈ 70 nm, obtained by structure factor of the two polymer blends, was formed by a combination of low crystallinity donor and acceptor pair, as crystallization-induced phase separation was suppressed.

The relative domain purity of each conjugated polymer blend is calculated based on total scattering intensity (TSI).^[12] The domain

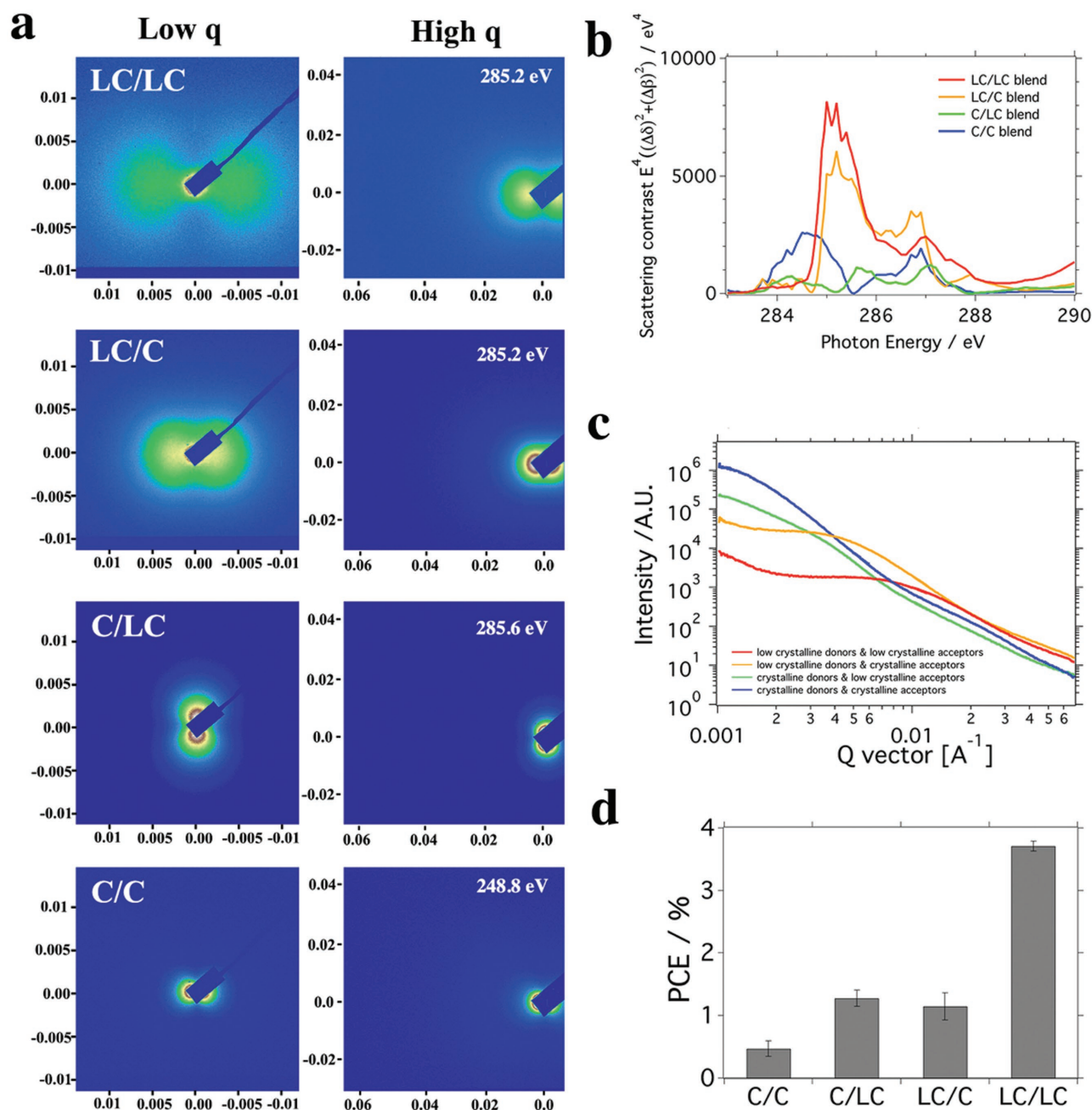


Figure 3. RSoXS characterization of the ternary films. The phase separation size scale of the all-polymer solar cells is highly dependent on crystallinity of donor and acceptor polymer. a) 2D RSoXS results for the four polymer blends. b) Plot of RSoXS scattering contrast between donor and acceptor polymer at different energy, assuming the polymer has a density of 1.1 g cm^{-3} . c) Scattering intensity versus scattering vector plot for the four polymer blends at their highest scattering contrast for each combination. The scattering profile at 270 eV is provided in Figure S4 (Supporting Information). d) Device performance for four different polymer blends. The phase separation size scale was found to be closely linked to the device performance. The film thickness for all samples is similar in this comparison.

purity calculation is discussed in detail in Figure S4 (Supporting Information). We found that with strong crystalline donor materials (PII2T), the domain purity is relatively high. The PII2T-PS/PNDIT showed 60% lower domain purity and the PII2T-PS/PPDIT showed 78% lower domain purity compared to two crystalline polymer blends, since the amorphous polymers are more likely to intermix each other (Table S2, Supporting Information).

2.3. Solar Cell Characterization

To illustrate the influence of morphology on photophysical properties, solar cells based on the above donor/acceptor blends were fabricated by spin-coating inks on glass/indium-doped tin oxide (ITO)/ZnO (30 nm) substrates, and subsequent thermal evaporation of MoO_3 (15 nm) and Ag (150 nm) as the top

Table 1. Device performance for all-polymer solar cells based on different degree of crystallinity.

| Materials | PCE [%] | J_{sc} [mA cm ⁻²] | V_{oc} [V] | FF | Phase separation ^{a)} [nm] | Relative domain purity ^{b)} |
|----------------|---------|---------------------------------|--------------|------|-------------------------------------|--------------------------------------|
| PII2T+PNDIT | 0.47 | 1.14 | 0.88 | 0.47 | >600 | 0.89 |
| PII2T+PPDIT | 1.28 | 2.90 | 0.88 | 0.50 | >600 | 1 |
| PII2T-PS+PNDIT | 1.15 | 3.15 | 0.83 | 0.44 | 150 | 0.40 |
| PII2T-PS+PPDIT | 3.71 | 8.51 | 0.87 | 0.50 | 70 | 0.22 |

^{a)}The structure factor of the blend polymer system is obtained from Bragg relation using the peak from the corresponding $l \times q \times q$ versus q plots (vertical sector). Both plots are shown in Figure S5 (Supporting Information); ^{b)}Domain purity calculation is based on the total scattering intensity of polymer blend from RSoXS measurement (Table S2, Supporting Information).

electrode. The PCEs of the all-polymer solar devices are shown in Table 1 and Figure 3d, comparing different phase separation size scales. The performance follows a trend closely associated with the phase separation size scale between the donor and acceptor. Using a low crystallinity donor/acceptor blend is found to be effective for reducing the phase separation size scale and thus such a blend also showed an enhanced solar cell performance.

Based on the above morphology and device studies, we found that tuning the crystallinity offers a simple way to suppress unfavorable phase separation between the donor and acceptor polymer. Using a low crystalline donor/acceptor pair gives the smallest phase separation size scale, which is important for efficient exciton splitting at donor/acceptor interfaces as can be seen by the increase in J_{sc} .

2.4. Low Crystallinity D/A Blend Morphology Insensitive to Process Conditions

Next, we performed solution printing of all-polymer solar cells. We first used a solution shearing coater to investigate the polymer morphology for PII2T-PS and PPDIT blends. The solution shearing coater has the benefit of having the same meniscus-guided drying process which closely resembled the R2R slot die coater, but uses only 10 μ L of solution per processing condition. Typically, 10 mg of conjugated polymer is sufficient to screen different processing conditions to obtain optimized device morphology with solution shearing. This is highly advantageous as large-scale reproducible and inexpensive synthesis of polymer remains a topic of research.^[42] The active layers, PII2T-PS and PPDIT, were solution-sheared at various speeds from their chlorobenzene or toluene solutions on the electron-transporting zinc oxide layer on ITO/glass. The ZnO layer was fabricated by spin-coating of a sol-gel ZnO precursor.^[56]

First, we observed a strong dependence of the film thickness on the solution shearing speeds in two distinct regions. At a lower shearing speed, for example, slower than 0.5 mm s⁻¹, the thickness of the solid films decreases with increasing shearing speed, as shown in Figure 4a. This is called the evaporation region, where the meniscus drying rate is similar as the coating speed. The surface tension of the ink is strong enough to hold

the meniscus along the moving blade. At a slower shearing speed, the meniscus is near the drying front and a thicker film is formed. When shearing speed is higher than 5 mm s⁻¹, the trend is reversed and the dried film thickness increased with increasing shearing speed. This is called the Landau–Levich region, in which the fast moving blade leaves behind a wet film with a drying similar to a drop-cast film. Typically, the morphology obtained from these two regimes is different due to different drying time, dynamics, and shearing force. However, in this case with the two low crystallinity polymer blends, there is not much difference in the performance of the devices sheared from those two different regions are not much different if the film thicknesses of two devices are similar. The J_{sc} reaches the maximum when the film thickness is 90 nm. In thicker film the absorption increases, however, more recombination of charge carriers also takes place. Thus, as the film thickness increases from 90 to 150 nm, the J_{sc} remains the same even though the absorption is slightly different. The integrated photocurrent from external quantum efficiency (EQE) data (Figure 4c,d) matches with the photocurrent obtained from a solar simulator.

The phase separation size between the donor and acceptor in the polymer blends was again examined by RSoXS. The 2D RSoXS images are shown in Figure S6 (Supporting Information). The anisotropic scattering profile is similar to isoindigo-based polymer due to slightly aligned polymer chains from solution shearing, as discussed in previous section. The scattering image was then reduced to intensity versus scattering vector and shown in Figure 4b. The shape of the scattering profiles is almost identical with different shearing speeds, showing that the phase separation between different processing conditions does not change. Since the phase separation length scales are similar, the efficiency of exciton dissociation should be the same. Thus, we conclude that the strong correlation between the film thickness and the J_{sc} is due to the insensitivity of the morphology to different processing conditions.

The fact that such a stable morphology can be obtained despite different coating speeds is attributed to the low crystallinity of the donor and acceptor polymers. Previously, morphology control of solution-processed solar cells has focused on polymer/fullerene BHJs.^[57] The PCBM-based solar cells have shown strong dependence on processing conditions due to fast diffusion of PCBM. This is understandable as PCBM is a small molecule that has a high diffusion coefficient compared to polymers.^[58] Thus, controlling the morphology of the final device is rather difficult in polymer:fullerene BHJs due to different drying process. Different techniques have been used to optimize the morphology, including additives,^[59] solvent treatment, and thermal treatments.^[57] In contrast, the highly stable morphology of our all-polymer BHJs is likely due to several reasons. First, the irregular polymer side chain is the key for inhibiting polymers from phase separation due to crystallization. Second, the relatively high molecular weight that we used results in highly entangled donor and acceptor polymer chains, which further slows down the spontaneous phase segregation. To take advantage of this effect, a relatively high molecular weight donor or acceptor polymer is required as polymer chain's diffusion rate is reduced with longer chain length. In this work, the molecular weight was measured by

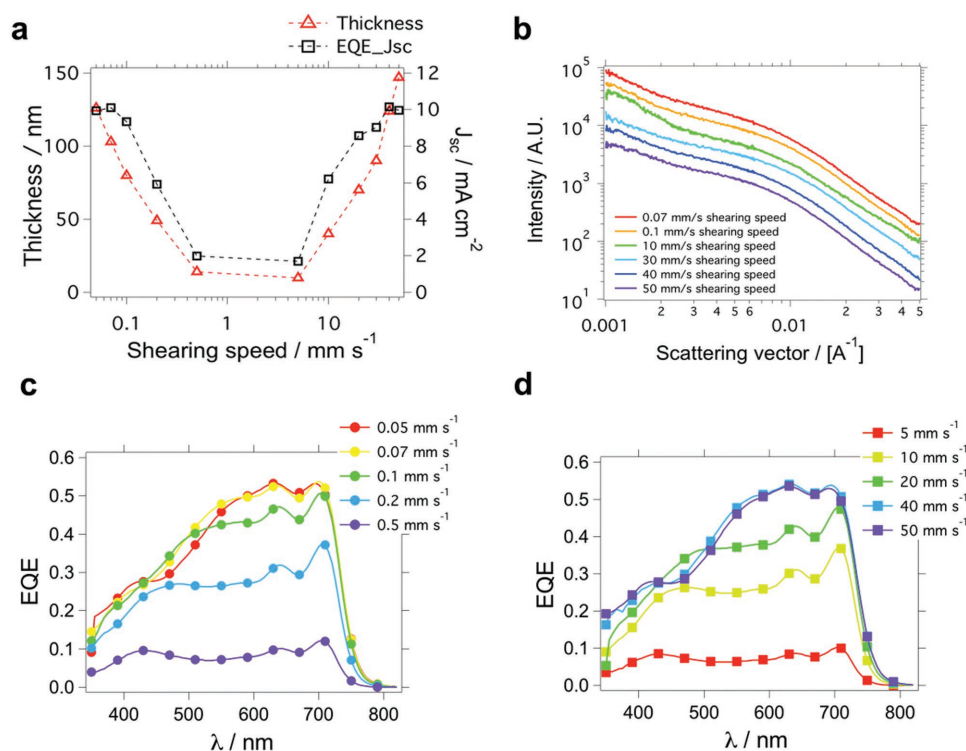


Figure 4. Morphology and device characteristic for solution sheared all-polymer solar cells. a) Film thickness and short circuit solar cell device current, J_{SC} at different shearing speeds. b) RSoXS for all-polymer solar cells printed at different speeds in the evaporation regime and Landau–Levich regime. EQE plots of solar cell devices printed at different speeds in the c) evaporation regime and d) Landau–Levich regime. A stable all-polymer morphology that is insensitive to different solution-processing conditions was observed.

high-temperature size exclusion chromatography (SEC). PII2T-PS has a M_n of 40 kDa. The donor polymer solution easily gels when it is left at room temperature overnight. High molecular weight polymer may also have the added benefit of reduced crystallinity as observed by other groups.^[60,61] To achieve a long-term stable solar cell under sunlight is more challenging since the stability of organic solar cell not only depends on the phase separation size scale but also the interactional layer between the electrode and active film, as well as photostability of semi-conducting polymers.

2.5. R2R Printing of All-Polymer Solar Cells

After the above investigation of printed polymer solar cells using the solution shearing coater, we scaled up the process by using R2R printing. Since our low crystallinity all-polymer solar cell blends showed very stable morphology during solution shearing with different shearing conditions, this morphology is ideal for R2R coating. We custom-built a mini R2R coater in our lab as shown in **Figure 5a**. Our group previously reported the implementation of this coater in a synchrotron beamline for real-time X-ray diffraction to perform in situ polymer morphology studies.^[62] A flexible polyethylene terephthalate (PET)/indium tin oxide (ITO) substrate is used as the substrate/bottom electrode. The ink was delivered via a syringe pump through a polytetrafluoroethylene (PTFE) tube to a slot die coater head. The thickness of the R2R printed film is

controlled by varying the syringe pump feed rate and substrate web speed. A ZnO layer was first printed, followed by the BHJ blend layer.

First, the electron transporting ZnO layer was optimized for the R2R printing process. A commercially available source (Infinity PV Inc.) was used. An ≈ 30 nm thickness was found to be the best for device performance. The detailed study for optimizing the ZnO layer is reported in the Supporting Information. Next, the active layer thickness was varied from 50 to 120 nm at a fixed ZnO thickness of 30 nm. We found that an active BHJ film thickness of ≈ 100 nm gave the best device performance. The thickness of the coated BHJ film can be monitored by the absorption intensity of the film, which indicated that a less than 4% variation in thickness was achieved over meters long continuously coated film, as shown in **Figure S8** and **Video S1** (Supporting Information). The top electrode was thermally evaporated with 15 nm MoO_3 as the hole transport layer and 150 nm Ag as the anode. The final device has an overall large device area consisting of individual pixels of 0.12 cm^2 as shown in **Figure 5c**. All the active pixel devices are connected to form accumulated area of 10 cm^2 solar cell device. We highlight the fact that the maximum printed device area is not limited to 10 cm^2 due to the continuous nature of R2R printing. The size limitation for the device in our lab is due to the size of the thermal evaporator. The device showed an average PCE of 4.1% over 12 measured cells and the best PCE of 4.24%. The J_{SC} was 9.58 mA cm^{-2} , V_{OC} was 0.989 V, and the FF was 0.45, which is slightly lower than the

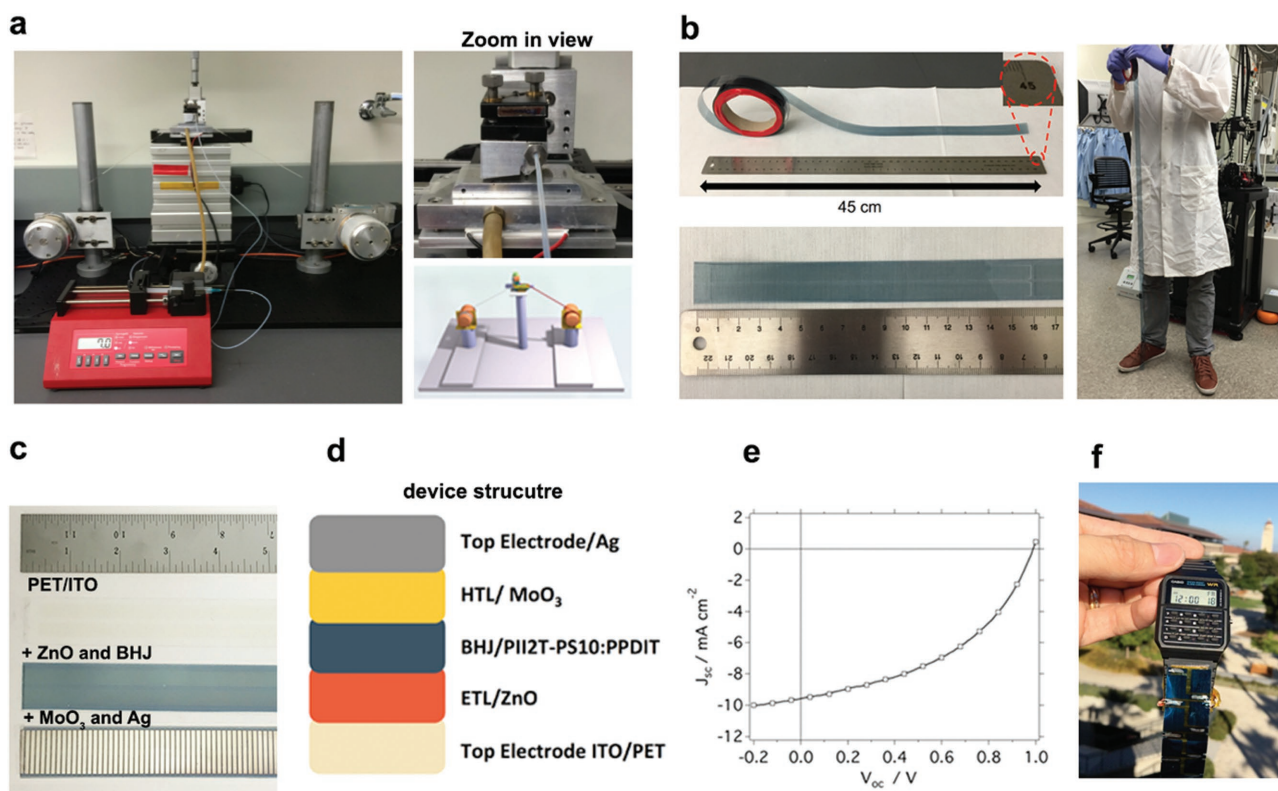


Figure 5. R2R printing of large-area solar cells. a) Photograph of the R2R printer setup. A zoom-in view of the slot die coater is also shown. b) Photograph of a printed roll of solar cell with ZnO and active layer. c) Photograph of solar cell during the fabrication process. From top to bottom the photos are PET/ITO substrate, substrate after coated with ZnO and BHJ layer, and complete device after MoO₃ and silver top electrode deposition. d) Sketch of the structure for the R2R-printed solar cells. e) J - V curve of a champion R2R-printed solar cell tested in a glove box under AM 1.5G simulated sunlight. f) A photo of an electronic watch powered by R2R-coated flexible solar cells.

solution-sheared device. We demonstrated the use of a R2R-printed flexible all-polymer solar cell to power an electronic watch under sunlight (as shown in Figure 5f, and Video S2, Supporting Information).

2.6. Extending the Selection Criteria to Other Polymers for R2R-Coated All-Polymer Solar Cells

The above work suggests that the selection of low crystallinity donor and acceptor polymers is highly desirable for R2R fabrication of solar cells since it results in smaller domain sizes and stable coating morphology regardless of coating speed. We tested another polymer combination of PTB7-Th,^[12,63–65] which is a low crystallinity donor, together with PNDIOD-T2 (or N2200), a highly crystalline acceptor.^[66] The fabricated cells did not perform well. The RSoXS scattering profile for PTB7-Th/PNDIOD-T2 mostly concentrated in the low q scattering area, indicating large phase separation between the donor and acceptor, larger than 300 nm, which most likely due to crystalline nature of the acceptor polymer (Figure S9, Supporting Information). We then selected another acceptor polymer with a PDI core copolymerized with vinyl group, PPDIE, as the acceptor polymer with PTB7-Th (Figure 6a).^[21] This acceptor polymer showed more disordered morphology as indicated by

the weak diffraction pattern (Figure 6b). The observed phase separation size was indeed smaller compared to PNDIOD-T2, as evidenced by the shoulder at 0.015 Å⁻¹ (Figure 6c). This donor/acceptor combination generated a higher J_{SC} , due to good spectrum coverage of the donor polymer and slightly improved fill factor due to improved charge mobility, despite a drop in the V_{OC} . The R2R-coated device showed an average PCE of 5.0% and a maximum PCE of 5.1%. The J_{SC} is 15.5 mA cm⁻², V_{OC} is 0.64 V, and FF is 0.50 (Figure 6d). A histogram of the device performance is shown in Figure 6e. The cell performance was also verified in another coauthor's lab, which confirmed the obtained performance of the solar cells as shown in Figure S11 (Supporting Information). This R2R slot die continuously printed active layer on flexible substrate is highest reported up to date (Figure 6f).

2.7. Conclusion

Our detailed morphology study for donor and acceptor polymers provides a way to understand phase separation behavior of conjugated polymers during solution printing. Since polymer crystallization serves as the driving force for phase separation, suppression of donor or acceptor polymer crystallization can prevent formation of large domains. We found that attaching

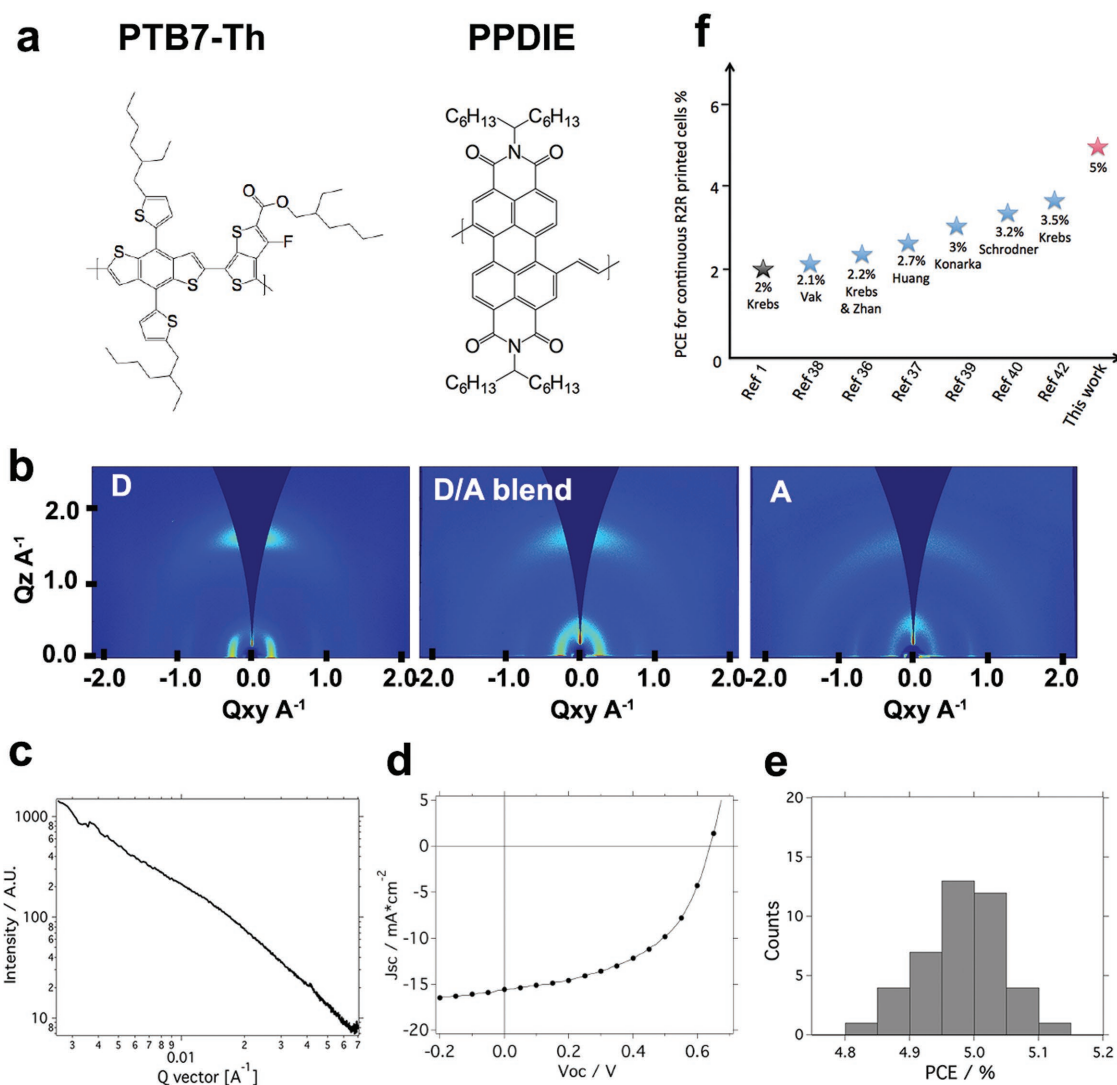


Figure 6. Morphology and device characteristics of another R2R-printed all-polymer solar cells. a) Chemical structures of PTB7-Th and PPDIE polymer. b) GIXD diffraction patterns for PTB7-Th, PTB7-Th/PPDIE, and PPDIE. c) RSoXS scattering profile for PTB7-Th/PPDIE BHJs at 287 eV. The scattering profile at 270 eV is shown in Figure S10 (Supporting Information). d) J–V curve of the champion PTB7-Th/PPDIE solar cell device. e) A histogram of device performance for all-polymer solar cells. f) A comparison of the performance with previous reported R2R continuous printed solar cells.^[1,36–40,42] Note the R2R device reported by Krebs group was fully R2R printed including Ag back electrode. A detailed table about fabrication method, device area, and device performance is provided in Table S7 (Supporting Information).

a bulky irregular PS side chain provides a way to fine-tune the phase separation size scale between the donor and acceptor polymers. The majority of poorly ordered polymer blends here showed highly stable morphology that is insensitive to different processing conditions. This characteristic showed great benefit for scaling up from a lab-scale solution shearing process to R2R printing. Continuously R2R-printed all-polymer solar cells with efficiency up to 5% are reported here. Even though this value is not the highest all-polymer solar cell performance, it is among the highest for R2R-coated active layer. The higher performing organic solar cells, on the other hand, remain to be spin-coated film with moderate crystallinity while additives tune the domain size and fast drying. Further understanding is still needed to develop an effective strategy to R2R coat such system reproducibly without compromised performance.

3. Experimental Section

Materials: PTB7-Th polymer was purchased from 1-Material and used as received. All other polymers were synthesized according to previously reported procedures.^[15] The donor polymers (PII2T and PII2T-PS) and acceptor polymers (PNDIT, PNDIO-T2, PPDI, and PPDIE) were purified via preparative size exclusion chromatography at room temperature. The M_n and D_M of polymers were measured by high-temperature GPC with 1,2,4-trichlorobenzene as the eluent and polystyrenes as the calibration standards at 180 °C, and were provided in the Supporting Information.

Morphology Characterizations: In situ GIXD images were collected in reflection mode with a 2D Pilatus 300k area detector in air at beamline 7-2 of the Stanford Synchrotron Radiation Lightsource (SSRL). The sample-to-detector distance was 360 mm, and the incidence angle was 0.12°; the X-ray wavelength was 0.8283 Å, corresponding to a beam energy of 15 keV. The samples were solution sheared from 15 mg mL⁻¹ chlorobenzene solvent at 35 °C at various printing speeds. The substrate

used for both sets of samples was bare Si wafer. Data analysis was performed using the Nika package inside Igor Pro by Jan Ilavsky (<http://usaxs.xray.aps.anl.gov/staff/ilavsky/nika.html>).

Ex situ GIXD images were collected in reflection mode with a 2D area detector in a helium chamber at beamline 11-3 of the SSRL. The sample-to-detector distance was 400 mm, and the incidence angle was 0.12° ; the X-ray wavelength was 0.9758 \AA , corresponding to a beam energy of 12.7 keV. The samples were solution sheared on bare Si wafers with a thin layer of native oxide. The data were processed using Wxdiff, written by Stefan Mannsfeld.

RSoXS data were collected at Advanced Light Source (ALS) beamline 11.0.1.2 in transmission geometry under vacuum. For sample preparation, Si wafers were first spin-coated with poly(sodium 4-styrenesulfonate) (PSS) 10 wt% aqueous solution at 5000 rpm for 30 s. The substrates were then baked in air at 100°C for 5 min to remove residual water. The desired BHJ ink was solution sheared or spin-coated on the PSS-coated Si wafer from 15 mg mL^{-1} chlorobenzene solution at 35°C , then floated off in deionized water and picked up onto 100 nm Si_3N_4 membranes (Norcada Inc.). The film was then dried in air before being transferred into the vacuum chamber for RSoXS measurement. NEXAFS were taken from 270 to 350 eV and used to calculate the energy-dependent optical constants.^[67] The contrast between two polymers was calculated from these and the scattering images were taken by a 2D CCD camera in vacuum at -45°C (Princeton Instrument PI-MTE). Scattering data were collected at two sample-to-detector distances of 50 and 150 mm to give a combined q range of $0.001\text{--}0.070 \text{ \AA}^{-1}$. Data analysis was also performed using the Nika package supported in the Igor Pro environment.^[68]

Solar Cell Fabrication and Testing Device Fabrication on Glass Substrates: Glass substrates with patterned ITO with a sheet resistance of $13 \Omega \square^{-1}$ were purchased from Xin Yan Technology Ltd. Before device fabrication, the ITO/glass substrate was ultrasonicated sequentially in acetone, detergent, deionized water, and isopropanol. The substrate was dried in a vacuum oven at 80°C for 10 min and cleaned by a 20 min UV-ozone treatment. A sol-gel solution of zinc hydroxide in ammonium was spin-coated onto the ITO surface at a speed of 5000 rpm for 30 s. The film was baked at 90°C for 10 min in air to form a 10 nm thick ZnO film. The polymers were dissolved in chlorobenzene and stirred for at least 3 h. The concentration was 10 mg mL^{-1} for donor and acceptors combined (1:1 ratio by weight). The solution was filtered with a $0.45 \mu\text{m}$ PTFE syringe filter prior to shearing. Solution shearing was performed at substrate temperature of 35°C . A side camera was used in the transmission geometry to align the blade to the substrate. The blade was slightly tilted and the printing was done at different speeds. After film preparation, the samples were transferred to a vacuum evaporator for electrode deposition. A MoO_3 layer (15 nm) followed by an Ag layer (150 nm) were thermally deposited at a pressure of 8×10^{-6} Torr.

Device Fabrication on R2R-Processed Flexible Substrates: ITO on PET substrate was patterned by photolithography to form the bottom electrode. During the R2R coating process, a ZnO layer was first coated on to the ITO/PET substrate. Then the active layer was coated on the top of the dried ZnO layer. The ZnO or solar cell ink was fed through a PTFE tube with 0.5 mm inner diameter by a syringe pump. The slot die coater was custom made and was mounted on the top of the PET substrate. The gap between the slot die and PET substrate was fixed at $250 \mu\text{m}$. A magnetic tension controller was coupled to the feeding roll and used to control the flatness of the PET substrate. The R2R setup was placed inside a laminar flow hood to minimize dust. During the R2R printing process, the speed of the syringe pump and the substrate motor were varied to achieve the desired film thickness with high uniformity. The speed of the substrate was controlled by the motor controller and varied from 0.36 to 0.72 m min^{-1} . The coated film was naturally dried under ambient conditions. After printing, the samples were transferred to a vacuum evaporator for electrode deposition. A MoO_3 layer (15 nm) followed by an Ag layer (150 nm) were thermally deposited at a pressure of 8×10^{-6} Torr.

All devices were tested inside a nitrogen glove box under AM 1.5G illumination with an intensity of 100 mW cm^{-2} (Newport Solar Simulator

94021A) calibrated by a Newport certified silicon photodiode covered with a KG5 filter. The photodiode active area was 6.63 mm^2 , which is comparable to the device area of 4.0 and 12 mm^2 . The J - V curves were recorded with a Keithley 2400 semiconductor analyzer. The connected solar cell module with active area of 10 cm^2 was tested in direct sunlight in Stanford, CA at noon in August, 2016. The intensity of the natural sunlight was also calibrated by a Newport certified silicon photodiode covered with a KG5 filter.

Supporting Information

Supporting Information is available from the Wiley Online Library or from the author.

Acknowledgements

X.G., Y.Z., M.T., and Z.B. acknowledge support through the Bridging Research Interactions through the collaborative Development Grants in Energy (BRIDGE) program under the SunShot initiative of the Department of Energy program under Contract No. DE-FOA-0000654-1588. T.K. and Z.B. acknowledge support from the Office of Naval Research (N00014-14-1-0142). K.G. was supported by the Department of Defense (DoD) through the National Defense Science and Engineering Graduate Fellowship (NDSEG) Program. H.Y. acknowledges support from the National Science Foundation Materials Genome Program (Award No. 1434799). B.S. acknowledges the National Research Fund of Luxembourg for financial support (Project No. 6932623). F.M.-L. was partly supported by the Swiss National Science Foundation under the Early Mobility Postdoc Project No. P2ELP2_155355 and the Department of Energy Basic Science (USA) Grant No. DE-SC0016523. D.Z. and Y.G. acknowledge the support from the National Natural Science Foundation of China (No.21674001 and 51473003). Y.L., H.L., and H.Y. thank Hong Kong Innovation and Technology Commission for the support through ITC-CNERC14SC01. In situ measurements were carried out at the Stanford Synchrotron Radiation Laboratory, a national user facility operated by Stanford University on behalf of the U.S. Department of Energy, Office of Basic Energy Sciences, under Contract No. DE-AC02-76SF00515. RSoXS experiments were performed at Advanced Light Source, which was supported by the Director, Office of Science, Office of Basic Energy Sciences, of the U.S. Department of Energy under Contract No. DE-AC02-05CH11231. The authors thank Bart Johnson for assistance during the in situ experiment at SSRL Beamline 7-2, and Nathan Ging-Ji Wang for performing high-temperature SEC measurements.

Received: December 8, 2016

Revised: January 12, 2017

Published online: March 7, 2017

- [1] F. C. Krebs, N. Espinosa, M. Hösel, R. R. Søndergaard, M. Jørgensen, *Adv. Mater.* **2014**, *26*, 29.
- [2] A. Polman, M. Knight, E. C. Garnett, B. Ehrler, W. C. Sinke, *Science* **2016**, *352*, 4424.
- [3] R. Søndergaard, M. Hösel, D. Angmo, T. T. Larsen-Olsen, F. C. Krebs, *Mater. Today* **2012**, *15*, 36.
- [4] N. Espinosa, M. Hösel, D. Angmo, F. C. Krebs, *Energy Environ. Sci.* **2012**, *5*, 5117.
- [5] Y. Liu, J. Zhao, Z. Li, C. Mu, W. Ma, H. Hu, K. Jiang, H. Lin, H. Ade, H. Yan, *Nat. Commun.* **2014**, *5*, 5293.
- [6] J. Zhao, Y. Li, G. Yang, K. Jiang, H. Lin, H. Ade, W. Ma, H. Yan, *Nat. Energy* **2016**, *1*, 15027.
- [7] W. Zhao, D. Qian, S. Zhang, S. Li, O. Inganäs, F. Gao, J. Hou, *Adv. Mater.* **2016**, *28*, 4734.

- [8] C. J. Brabec, M. Heeney, I. McCulloch, J. Nelson, *Chem. Soc. Rev.* **2011**, *40*, 1185.
- [9] H. W. Ro, J. M. Downing, S. Engmann, A. A. Herzing, D. M. DeLongchamp, L. J. Richter, S. Mukherjee, H. Ade, M. Abdelsamie, L. K. Jagadamma, A. Amassian, Y. Liu, H. Yan, *Energy Environ. Sci.* **2016**, *9*, 2835.
- [10] Y. Tamai, H. Ohkita, H. Benten, S. Ito, *J. Phys. Chem. Lett.* **2015**, *6*, 3417.
- [11] B. A. Collins, J. R. Tumbleston, H. Ade, *J. Phys. Chem. Lett.* **2011**, *2*, 3135.
- [12] B. A. Collins, Z. Li, J. R. Tumbleston, E. Gann, C. R. McNeill, H. Ade, *Adv. Energy Mater.* **2013**, *3*, 65.
- [13] F. Liu, Y. Gu, X. Shen, S. Ferdous, H.-W. Wang, T. P. Russell, *Prog. Polym. Sci.* **2013**, *38*, 1990.
- [14] E. Verploegen, R. Mondal, C. J. Bettinger, S. Sok, M. F. Toney, Z. Bao, *Adv. Funct. Mater.* **2010**, *20*, 3519.
- [15] B. A. Collins, J. E. Cochran, H. Yan, E. Gann, C. Hub, R. Fink, C. Wang, T. Schuettfort, C. R. McNeill, M. L. Chabinyc, H. Ade, *Nat. Mater.* **2012**, *11*, 536.
- [16] E. Bundgaard, F. Livi, O. Hagemann, J. E. Carlé, M. Helgesen, I. M. Heckler, N. K. Zawacka, D. Angmo, T. T. Larsen-Olsen, G. A. dos Reis Benatto, B. Roth, M. V. Madsen, M. R. Andersson, M. Jørgensen, R. R. Søndergaard, F. C. Krebs, *Adv. Energy Mater.* **2015**, *5*, 1402186.
- [17] Y.-J. Hwang, B. A. E. Courtright, A. S. Ferreira, S. H. Tolbert, S. A. Jenekhe, *Adv. Mater.* **2015**, *27*, 4578.
- [18] L. Gao, Z.-G. Zhang, L. Xue, J. Min, J. Zhang, Z. Wei, Y. Li, *Adv. Mater.* **2016**, *28*, 1884.
- [19] Z. Li, X. Xu, W. Zhang, X. Meng, W. Ma, A. Yartsev, O. Inganäs, M. R. Andersson, R. A. J. Janssen, E. Wang, *J. Am. Chem. Soc.* **2016**, *138*, 10935.
- [20] L. Ye, X. Jiao, W. Zhao, S. Zhang, H. Yao, S. Li, H. Ade, J. Hou, *Chem. Mater.* **2016**, *28*, 6178.
- [21] Y. Guo, Y. Li, O. Awartani, J. Zhao, H. Han, H. Ade, D. Zhao, H. Yan, *Adv. Mater.* **2016**, *28*, 8483.
- [22] Y. Zhou, T. Kurosawa, W. Ma, Y. Guo, L. Fang, K. Vandewal, Y. Diao, C. Wang, Q. Yan, J. Reinspach, J. Mei, A. L. Appleton, G. I. Koleilat, Y. Gao, S. C. B. Mannsfeld, A. Salleo, H. Ade, D. Zhao, Z. Bao, *Adv. Mater.* **2014**, *26*, 3767.
- [23] Y. Diao, Y. Zhou, T. Kurosawa, L. Shaw, C. Wang, S. Park, Y. Guo, J. A. Reinspach, K. Gu, X. Gu, B. C. K. Tee, C. Pang, H. Yan, D. Zhao, M. F. Toney, S. C. B. Mannsfeld, Z. Bao, *Nat. Commun.* **2015**, *6*, 7955.
- [24] T. Kim, J.-H. Kim, T. E. Kang, C. Lee, H. Kang, M. Shin, C. Wang, B. Ma, U. Jeong, T.-S. Kim, B. J. Kim, *Nat. Commun.* **2015**, *6*, 1.
- [25] K. D. Deshmukh, T. Qin, J. K. Gallaher, A. C. Y. Liu, E. Gann, K. O'Donnell, L. Thomsen, J. M. Hodgkiss, S. E. Watkins, C. R. McNeill, *Energy Environ. Sci.* **2014**, *8*, 332.
- [26] J. R. Moore, S. Albert-Seifried, A. Rao, S. Massip, B. Watts, D. J. Morgan, R. H. Friend, C. R. McNeill, H. Sirringhaus, *Adv. Energy Mater.* **2011**, *1*, 230.
- [27] H. Yan, B. A. Collins, E. Gann, C. Wang, H. Ade, C. R. McNeill, *ACS Nano* **2012**, *6*, 677.
- [28] X. Gu, H. Yan, T. Kurosawa, B. C. Schroeder, K. L. Gu, Y. Zhou, J. W. F. To, S. D. Oosterhout, V. Savikhin, F. Molina-Lopez, C. J. Tassone, S. C. B. Mannsfeld, C. Wang, M. F. Toney, Z. Bao, *Adv. Energy Mater.* **2016**, *6*, 1601225.
- [29] A. J. Heeger, *Adv. Mater.* **2013**, *26*, 10.
- [30] E. Verploegen, C. E. Miller, K. Schmidt, Z. Bao, M. F. Toney, *Chem. Mater.* **2012**, *24*, 3923.
- [31] G. Li, Y. Yao, H. Yang, V. Shrotriya, G. Yang, Y. Yang, *Adv. Funct. Mater.* **2007**, *17*, 1636.
- [32] A. Sharenko, N. D. Treat, J. A. Love, M. F. Toney, N. Stingelin, T.-Q. Nguyen, *J. Mater. Chem. A* **2014**, *2*, 15717.
- [33] N. D. Treat, J. A. N. Malik, O. Reid, L. Yu, C. G. Shuttle, G. Rumbles, C. J. Hawker, M. L. Chabinyc, P. Smith, N. Stingelin, *Nat. Mater.* **2013**, *12*, 628.
- [34] A. Buzarovska, *Polym. Int.* **2005**, *54*, 1466.
- [35] R. J. Kline, M. D. McGehee, E. N. Kadnikova, J. Liu, J. M. J. Fréchet, M. F. Toney, *Macromolecules* **2005**, *38*, 3312.
- [36] K. Liu, T. T. Larsen-Olsen, Y. Lin, M. Beliatas, E. Bundgaard, M. Jørgensen, F. C. Krebs, X. Zhan, *J. Mater. Chem. A* **2016**, *4*, 1044.
- [37] Y.-C. Huang, H.-C. Cha, C.-Y. Chen, C.-S. Tsao, *Sol. Energy Mater. Sol. Cells* **2016**, *150*, 10.
- [38] D. Vak, H. Weerasinghe, J. Ramamurthy, J. Subbiah, M. Brown, D. J. Jones, *Sol. Energy Mater. Sol. Cells* **2016**, *149*, 154.
- [39] F. Yan, J. Noble, J. Peltola, S. Wicks, S. Balasubramanian, *Sol. Energy Mater. Sol. Cells* **2013**, *114*, 214.
- [40] M. Schrödner, S. Sensfuss, H. Schache, K. Schultheis, T. Welzel, K. Heinemann, R. Milker, J. Marten, L. Blankenburg, *Sol. Energy Mater. Sol. Cells* **2012**, *107*, 283.
- [41] B. Roth, G. A. dos Reis Benatto, M. Corazza, J. E. Carlé, M. Helgesen, S. A. Gevorgyan, M. Jørgensen, R. R. Søndergaard, F. C. Krebs, *Adv. Eng. Mater.* **2016**, *18*, 511.
- [42] M. Helgesen, J. E. Carlé, G. A. dos Reis Benatto, R. R. Søndergaard, M. Jørgensen, E. Bundgaard, F. C. Krebs, *Adv. Energy Mater.* **2015**, *5*, 1401996.
- [43] T. R. Andersen, H. F. Dam, M. Hösel, M. Helgesen, J. E. Carlé, T. T. Larsen-Olsen, S. A. Gevorgyan, J. W. Andreasen, J. Adams, N. Li, F. Machui, G. D. Spyropoulos, T. Ameri, N. Lemaitre, M. Legros, A. Scheel, D. Gaiser, K. Kreul, S. Berny, O. R. Lozman, S. Nordman, M. Välimäki, M. Vilkmann, R. R. Søndergaard, M. Jørgensen, C. J. Brabec, F. C. Krebs, *Energy Environ. Sci.* **2014**, *7*, 2925.
- [44] G. Reiter, *Chem. Soc. Rev.* **2014**, *43*, 2055.
- [45] I. McCulloch, M. Heeney, C. Bailey, K. Genevicius, I. MacDonald, M. Shkunov, D. Sparrowe, S. Tierney, R. Wagner, W. Zhang, M. L. Chabinyc, R. J. Kline, M. D. McGehee, M. F. Toney, *Nat. Mater.* **2006**, *5*, 328.
- [46] J. Rivnay, S. C. B. Mannsfeld, C. E. Miller, A. Salleo, M. F. Toney, *Chem. Rev.* **2012**, *112*, 5488.
- [47] R. Noriega, J. Rivnay, K. Vandewal, F. P. V. Koch, N. Stingelin, P. Smith, M. F. Toney, A. Salleo, *Nat. Mater.* **2013**, *12*, 1038.
- [48] H. Yang, T. J. Shin, L. Yang, K. Cho, C. Y. Ryu, Z. Bao, *Adv. Funct. Mater.* **2005**, *15*, 671.
- [49] R. Steyrlleuthner, R. Di Pietro, B. A. Collins, F. Polzer, S. Himmelberger, M. Schubert, Z. Chen, S. Zhang, A. Salleo, H. Ade, A. Facchetti, D. Neher, *J. Am. Chem. Soc.* **2014**, *136*, 4245.
- [50] K. A. Mazzio, A. H. Rice, M. M. Durban, C. K. Luscombe, *J. Phys. Chem. C* **2015**, *119*, 14911.
- [51] J. C. Sworen, J. A. Smith, J. M. Berg, K. B. Wagener, *J. Am. Chem. Soc.* **2004**, *126*, 11238.
- [52] J. L. Baker, L. H. Jimison, S. Mannsfeld, S. Volkman, S. Yin, V. Subramanian, A. Salleo, A. P. Alivisatos, M. F. Toney, *Langmuir* **2010**, *26*, 9146.
- [53] D. Chen, A. Nakahara, D. Wei, D. Nordlund, T. P. Russell, *Nano Lett.* **2011**, *11*, 561.
- [54] W. Ma, J. Reinspach, Y. Zhou, Y. Diao, T. McAfee, S. C. B. Mannsfeld, Z. Bao, H. Ade, *Adv. Funct. Mater.* **2015**, *25*, 3131.
- [55] F. Liu, C. Wang, J. K. Baral, L. Zhang, J. J. Watkins, A. L. Briseno, T. P. Russell, *J. Am. Chem. Soc.* **2013**, *135*, 19248.
- [56] Y. Sun, J. H. Seo, C. J. Takacs, J. Seifert, A. J. Heeger, *Adv. Mater.* **2011**, *23*, 1679.
- [57] Y. Huang, E. J. Kramer, A. J. Heeger, G. C. Bazan, *Chem. Rev.* **2014**, *114*, 7006.
- [58] N. D. Treat, M. A. Brady, G. Smith, M. F. Toney, E. J. Kramer, C. J. Hawker, M. L. Chabinyc, *Adv. Energy Mater.* **2010**, *1*, 82.

- [59] J. Peet, J. Y. Kim, N. E. Coates, W. L. Ma, D. Moses, A. J. Heeger, G. C. Bazan, *Nat. Mater.* **2007**, *6*, 497.
- [60] F. P. V. Koch, J. Rivnay, S. Foster, C. Müller, J. M. Downing, E. Buchaca-Domingo, P. Westacott, L. Yu, M. Yuan, M. Baklar, Z. Fei, C. Luscombe, M. A. McLachlan, M. Heeney, G. Rumbles, C. Silva, A. Salleo, J. Nelson, P. Smith, N. Stingelin, *Prog. Polym. Sci.* **2013**, *38*, 1978.
- [61] N. Zhou, A. S. Dudnik, T. I. N. G. Li, E. F. Manley, T. J. Aldrich, P. Guo, H.-C. Liao, Z. Chen, L. X. Chen, R. P. H. Chang, A. Facchetti, M. O. de la Cruz, T. J. Marks, *J. Am. Chem. Soc.* **2016**, *138*, 1240.
- [62] X. Gu, J. Reinspach, B. J. Worfolk, Y. Diao, Y. Zhou, H. Yan, K. Gu, S. Mannsfeld, M. F. Toney, Z. Bao, *ACS Appl. Mater. Interfaces* **2016**, *8*, 1687.
- [63] M. R. Hammond, R. J. Kline, A. A. Herzing, L. J. Richter, D. S. Germack, H. W. Ro, C. L. Soles, D. A. Fischer, T. Xu, L. Yu, M. F. Toney, D. M. DeLongchamp, *ACS Nano* **2011**, *5*, 8248.
- [64] F. Liu, W. Zhao, J. R. Tumbleston, C. Wang, Y. Gu, D. Wang, A. L. Briseno, H. Ade, T. P. Russell, *Adv. Energy Mater.* **2013**, *4*, 1301377.
- [65] H. Kang, K.-H. Kim, J. Choi, C. Lee, B. J. Kim, *ACS Macro Lett.* **2014**, *3*, 1009.
- [66] C. Mu, P. Liu, W. Ma, K. Jiang, J. Zhao, K. Zhang, Z. Chen, Z. Wei, Y. Yi, J. Wang, S. Yang, F. Huang, A. Facchetti, H. Ade, H. Yan, *Adv. Mater.* **2014**, *26*, 7224.
- [67] B. Watts, *Opt. Express* **2014**, *22*, 23628.
- [68] J. Ilavsky, *J. Appl. Crystallogr.* **2012**, *45*, 324.